# Screening Spinel Oxide Supports for RuO$_2$ to Boost Bifunctional Electrocatalysts for Advanced Zn–Air Batteries

*Xiaohong Zou, Qian Lu, Jie Wu, Kouer Zhang, Mingcong Tang, Baoxin Wu, Sixuan She, Xiao Zhang,\* Zongping Shao,\* and Liang An\**

The compositing strategy offers great potential in designing bifunctional oxygen electrocatalysts for Zn–air batteries. Recent reports reveal that the couple of RuO$_2$, serving as a benchmark oxygen evolution reaction (OER) catalyst, with other oxygen reduction reaction (ORR) catalysts is a wise choice to build highly efficient bifunctional electrocatalysts. However, the design criteria for ORR and OER activities of RuO$_2$-based composite catalysts are still unclear. Herein, a series of transition metal (Fe, Co, Mn, and Ni)-doped spinel oxides are designed to support RuO$_2$ nanorods for exploring the reaction mechanism. Through advanced technology, it is considered that increasing the content and binding energy of Co$^{3+}$ and enhancing the oxidation state of Ru$^{4+}$ is an efficient strategy to promote ORR and OER activities for RuO$_2$/Co-based spinel oxide composite catalysts. It is found that coupling Mn-doping Co$_3$O$_4$ (CMO) supports with RuO$_2$ can induce the highest catalytic activities in ORR/OER and excellent performance in rechargeable Zn–air batteries. Operando electrochemical impedance spectroscopy and theoretical calculation further prove the synergistic effect between RuO$_2$ and CMO supports originated from the oxygen overflow to overcome the large barrier for oxygen desorption on RuO$_2$ during OER and oxygen adsorption on CMO supports during ORR.

## 1. Introduction

Considering the urgent goal of "carbon neutralization" to tackle the matter of CO$_2$ emissions, rechargeable Zn–air batteries have obtained more attention in recent years among various energy storage and conversion devices (e.g., Li-ion batteries, Li–S batteries, fuel cells, and Li–air batteries), owing to its high theoretical energy density of 1218 Wh kg$^{-1}$, low cost, and improved safety, as well as environmental friendliness.[1] However, the commercialization of rechargeable Zn–air batteries has not yet been fully achieved owing to the sluggish reaction kinetics of oxygen-based electrochemistry on the air cathode, which results in large ORR/OER overpotentials and low energy efficiency.[2] Therefore, designing highly efficient oxygen electrocatalysts is a current hot research topic in the field of rechargeable Zn–air batteries.

Recently, many strategies, e.g., compositing,[3] doping,[4] defecting,[5] and straining engineering,[6] have been proposed to develop bifunctional electrocatalysts. Generally, ORR and OER require

X. Zou, J. Wu, K. Zhang, M. Tang, B. Wu, X. Zhang, L. An
Department of Mechanical Engineering
The Hong Kong Polytechnic University
Hung Hom, Kowloon, Hong Kong SAR P. R. China
E-mail: xiao1.zhang@polyu.edu.hk; liang.an@polyu.edu.hk

Q. Lu
Jiangsu Collaborative Innovation Center of Atmospheric Environment and Equipment Technology
Jiangsu Key Laboratory of Atmospheric Environment Monitoring and Pollution Control
School of Environmental Science and Technology
Nanjing University of Information Science and Technology
Nanjing 210044, P. R. China

Q. Lu
Department of Chemistry
The Chinese University of Hong Kong
Ma Lin building, Shatin 999077, P. R. China

S. She
Department of Applied Physics and Materials Research Center
The Hong Kong Polytechnic University
Hung Hom, Kowloon, Hong Kong SAR P. R. China

X. Zhang, L. An
Research Institute for Advanced Manufacturing
The Hong Kong Polytechnic University
Hung Hom, Kowloon, Hong Kong SAR P. R. China

Z. Shao
WA School of Mines: Minerals
Energy and Chemical Engineering (WASM-MECE)
Curtin University
Perth, WA 6845, Australia
E-mail: shaozp@njtech.edu.cn

L. An
Research Institute for Smart Energy
The Hong Kong Polytechnic University
Hung Hom, Kowloon, Hong Kong SAR P. R. China

**ADVANCED
SCIENCE NEWS**

www.advancedsciencenews.com

**ADVANCED
FUNCTIONAL
MATERIALS**

www.afm-journal.de

various catalytic sites located near the top of "volcanic curves" owing to the scaling relationship, thus single catalytic sites are unable to achieve excellent bifunctional activity simultaneously.[7] Researchers have shown that integrating two different catalytic sites into one catalyst can achieve both ORR and OER activities, meanwhile, two catalytic sites can induce a synergistic effect to enhance the catalytic activity owing to the optimization of electronic structure.[8] Many bifunctional oxygen electrocatalysts, such as $Fe_3Pt$-$Ni_3FeN$,[9] CoNC@NiFe-LDH,[10] NiFeMn trimetallic nitride/$Ti_3C_2$,[11] etc., have been designed by integrating two components. As reported, heterogeneous interfaces can regulate the electronic structure of two components and enhance the electron conduction during the reaction, thus greatly enhancing the ORR and OER activities.[12] Constructing suitable composite catalysts is crucial for the practicality of rechargeable Zn–air batteries.

$RuO_2$-based composite catalysts perform great potential in building bifunctional electrocatalysts given the excellent OER catalytic activity and the competitive price of $RuO_2$ compared to other noble metal catalysts.[13] Recent works reveal that loading $RuO_2$ onto appropriate oxide supports can regulate its ORR activity, which has achieved excellent performance on rechargeable Zn–air batteries.[14] To customize suitable supports for regulating the ORR/OER activity of $RuO_2$, we recently proposed using $Co_3O_4$ as support to load the $RuO_2$ nanocluster.[13b] The high-energy interfacial Ru-O-Co bond between $Co_3O_4$ and $RuO_2$ serves as the main catalytic site to promote ORR and OER. Since then, many similar composite catalysts, including $RuCoO_x$,[15] $Co_3O_4$-$RuO_2$,[16] Ru/$RuO_2$@NCS,[17] Co-$RuO_2$/OCNT,[7b] etc., have been reported in the field of rechargeable Zn–air batteries. Here two types of supports, oxide and carbon, were designed for $RuO_2$. As reported, the oxidation corrosion of carbon supports can easily affect the discharge performance.[18] In contrast, oxide supports, especially $Co_3O_4$, can maintain structure stability during the charging and discharging process, resulting in better energy efficiency retention.[19] However, there are still urgent to clarify the design criteria for ORR and OER activities of $RuO_2$-based composite catalysts to guide the design of such composite catalysts in the future.

In this work, we screen different Co-based spinel oxides via doping transition metal (Fe, Co, Mn, and Ni) to support $RuO_2$ nanorods through a simple sol-gel method. Among different composite catalysts, $RuO_2$/CMO performs a low overpotential gap of 0.74 V, which is better than corresponding single-phase catalysts and commercial Pt/C-$IrO_2$. XPS, operando EIS and DFT calculation prove the synergistic effect between $RuO_2$ and CMO supports, offering the main OER and ORR active sites, respectively, originating from the oxygen overflow to overcome the large barrier for oxygen desorption on $RuO_2$ during OER and oxygen adsorption on CMO supports during ORR. Especially, $RuO_2$/CMO assembled Zn–air batteries perform a high peak energy density and specific capacity of 211 mW $cm^{-2}$ and 755 mAh $g_{Zn}^{-1}$, respectively, and even an ultra-long lifespan of over 100 h at 10 mA $cm^{-2}$, outperforming commercial Pt/C-$IrO_2$ mixed catalysts. We believe that the design concept in constructing composite catalysts can provide a promising solution for building efficient bifunctional electrocatalysts.

## 2. Results and Discussion

To effectively screen the optimal Co-based spinel supports for $RuO_2$, we describe herein a simple sol-gel method for loading $RuO_2$ nanorods on a series of Co-based spinel oxides, including $Co_{1.5}Mn_{1.5}O_4$ (CMO), $Co_{1.5}Ni_{1.5}O_4$ (CNO), $Co_{1.5}Fe_{1.5}O_4$ (CFO), and $Co_3O_4$ (CCO). As schematically exhibited in **Figure 1a**, taking $RuO_2$ nanorods grown on CMO supports as an example, $RuO_2$ nanorods have been uniformly grown on CMO matrix by a simple sol–gel method with the subsequently sintering process in a muffle furnace. In brief, a homogeneous solution including citric acid monohydrate (CA), urea, $Co(NO_3)_2$, $Mn(NO_3)_2$, and $RuCl_3$ was heated with vigorously stirring at 200 °C for 5 h to form the gel, then annealed at 550 °C to remove the CA and urea template. X-ray diffraction (XRD) and Raman techniques were applied to characterize the crystalline structure and physical nature. As shown in Figure 1b–d, the peak at 28.1°, 35.2°, 40.2° and 54.4°, which respectively indexed to (110), (101), (200) and (211) planes of $RuO_2$ (PDF#00-021-1172), are existing for $RuO_2$ and $RuO_2$/CMO samples.[20] In addition, the main peaks located at 18.5°, 30.5°, 35.9°, 43.7°, 57.8°, and 63.5°, which respectively index to (111), (220), (311), (400), (511), and (440) planes of $MnCo_2O_4$ (PDF#01-084-0482), can be observed for CMO and $RuO_2$/CMO.[21] The result proves that the obtained $RuO_2$/CMO is composed of $RuO_2$ and spinel oxide phases. As for other spinel-supported induced composite catalysts, the diffraction peak of $RuO_2$ can also be observed in Figure S1 (Supporting Information). Besides, Co-based spinel oxides, including $NiCo_2O_4$ (PDF#01-073-1702),[22] $CoFe_2O_4$ (PDF#00-001-1121),[23] and $CoCo_2O_4$ (PDF#01-080-1535)[24] for $RuO_2$/CNO, $RuO_2$/CFO and $RuO_2$/CCO, respectively, can also be found, declaring that the sol-gel method is universal for preparing the composite catalyst. Raman spectra were further acquired as shown in Figure S2 (Supporting Information). The band located at ≈470, 620, and 675 $cm^{-1}$ belongs to $E_g$, $F_{2g}$, and $A_{1g}$ modes of Co—O bond in spinel oxide,[25] and two peaks at 624 and 510 $cm^{-1}$ belong to $A_{1g}$ and $E_g$ modes of the Ru—O bond in $RuO_2$.[26] The band for $RuO_2$ can be observed for all samples, revealing the existence of $RuO_2$. Particularly, the band of Co—O bonds has disappeared for $RuO_2$/CNO, $RuO_2$/CFO, and $RuO_2$/CMO owing to the long-range arrangement of Co—O bonds being disrupted by doping other transition metal ions.

There are two factors in the selection of urea, first, in precursor solution, urea can provide an alkaline environment to promote the formation of gel, second, during the calcination process, urea will decompose into gas products to construct a rich pore structure inside catalyst for avoiding the stacking of catalyst particles.[13a] The morphology of as-prepared catalysts was detected by field-emission scanning electron microscopy (SEM) to prove the function of urea. As displayed in Figure S3 (Supporting Information), both CMO and $RuO_2$/CMO perform porous foamlike structures aggregated by nanoparticles. This unique nanostructure with abundant pores favors the gas–solid–liquid (release of generated gases, the exposure of active sites, and the transport of electrolytes) three-phase transfer. We further applied transmission electron microscopy (TEM) to study the microstructure of $RuO_2$/CMO. As shown in Figure 1e and Figure S4 (Supporting Information), the $RuO_2$/CMO revealed a porous nanosheet structure, in which the $RuO_2$ nanorods with a
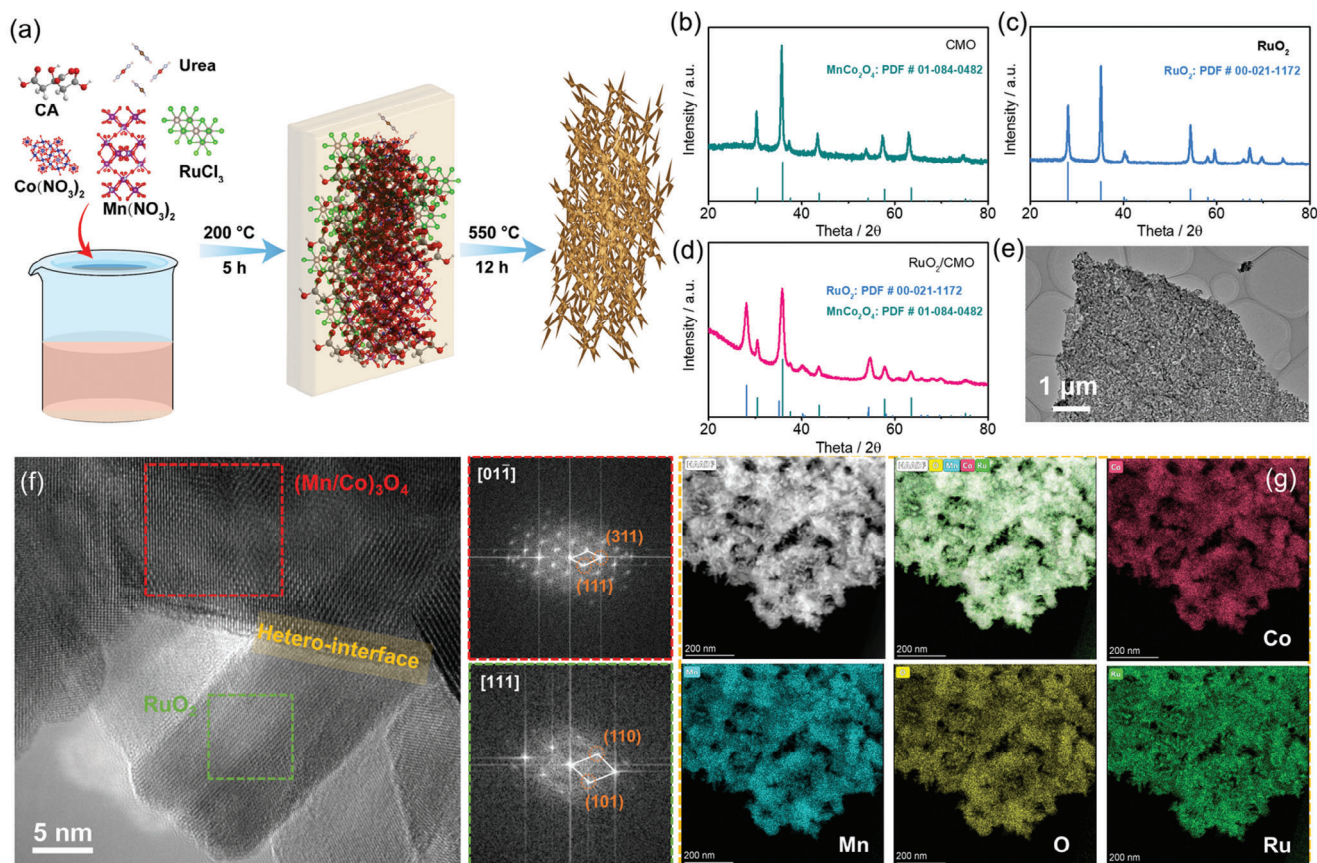
**Figure 1.** Synthesis and characterization of catalyst. a) Schematic illustration of the main fabrication procedure for RuO$_2$/CMO catalyst. XRD patterns of b) CMO catalyst, c) RuO$_2$ catalyst, and d) RuO$_2$/CMO catalyst. e–g) HRTEM image of RuO$_2$/CMO catalyst and its corresponding FFT images. g) HAADF-STEM image of RuO$_2$/CMO catalyst and corresponding mappings of Co, Mn, O, and Ru elements.

diameter size of ≈10 nm are homogeneously supported on the CMO surface. The crystal structure of catalysts was also explored by high-resolution transmission electron microscopy (HRTEM). We select a region that contains both nanorod and substrate in Figure 1f. These two regions perform different lattice fringe and obvious hetero-interface can be observed. We employed fast Fourier transform (FFT) technology to analyze the crystal structure of two regions. For the red box area, the lattice planes of (111) and (311) with lattice distances of 0.19 and 0.25 nm, respectively, are discovered, which corresponds to spinel oxide along the [01$\bar{1}$] direction.[27] For the green box area, we can detect two lattice planes that are associated with (110) and (101) planes of RuO$_2$ along [1$\bar{1}$1] direction.[28] Therefore, the RuO$_2$ nanorod was tightly supported on the CMO surface with an obvious hetero-interface in RuO$_2$/CMO. The corresponding elemental mappings result verifies the uniform distribution of Co, Mn, Ru, and O elements, further proving that the RuO$_2$ nanorod was uniformly supported on CMO supports (Figure 1g). Combining with the energy-dispersive X-ray spectroscopy (EDX) and inductively coupled plasma atomic emission spectroscopy (ICP-OES) results, the RuO$_2$ nanorod supported on CMO spinel oxides is successfully synthesized with the mole fraction of Co: Mn: Ru is ≈1: 1: 1, approaching the molar ratio of added metal ions, as illustrated in Figure S5 and Table S1 (Supporting In-

formation). Therefore, there is ≈35 wt.% Ru in RuO$_2$/CMO catalysts.

To screen the suitable Co-based supports for loading RuO$_2$ nanorods for creating bifunctional electrocatalysts, ORR and OER activities of different supported catalysts, including RuO$_2$/CNO, RuO$_2$/CFO, RuO$_2$/CCO, and RuO$_2$/CMO, were first investigated through a three-electrode device in O$_2$-staturated 0.1 M KOH electrolyte with rotating rate of 1600 rpm. As shown in **Figure 2a**, RuO$_2$/CMO catalyst delivered excellent ORR activity with a half-potential ($E_{1/2}$) of 0.80 V and high diffusion-limited current densities ($J_l$) of 5.2 mA cm$^{-2}$, which outperforms that of RuO$_2$/CCO ($E_{1/2}$ = 0.77 V, $J_l$ = 4.8 mA cm$^{-2}$), RuO$_2$/CFO ($E_{1/2}$ = 0.63 V, $J_l$ = 4.0 mA cm$^{-2}$), RuO$_2$/CNO ($E_{1/2}$ = 0.72 V, $J_l$ = 3.7 mA cm$^{-2}$). Then the Tafel slope was calculated from linear sweep voltammogram (LSV) curves in Figure S6 (Supporting Information) to evaluate the ORR reaction kinetics, in which a smaller value means a faster ORR electrochemical reaction. The Tafel slope value of RuO$_2$/CMO was just 68 mV dec$^{-1}$, which was lower than other supported catalysts, suggesting the fast reaction kinetics for combining RuO$_2$ and CMO. As the CV area related to the availability of active sites, the RuO$_2$/CMO catalyst exhibited more active sites for ORR reaction than the other catalysts, e.g., RuO$_2$/CCO, RuO$_2$/CNO, RuO$_2$/CFO, and other Co-based spinel oxides, originated from CV curves in Figure S7
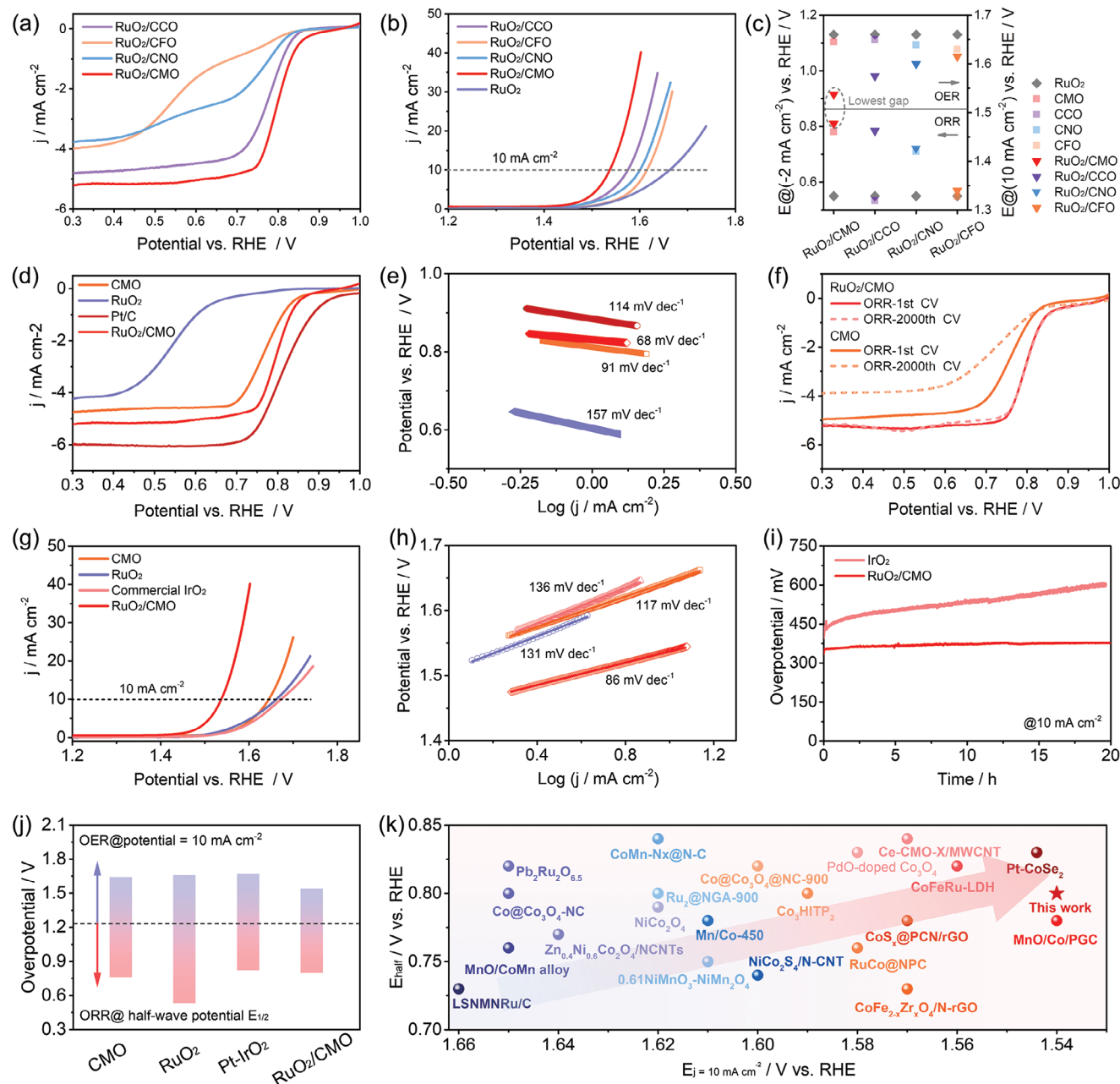
**Figure 2.** Electrochemical activity of catalyst. a) ORR LSV polarization curves for RuO$_2$/CCO, RuO$_2$/CFO, RuO$_2$/CNO, and RuO$_2$/CMO catalysts. b) OER LSV polarization curves for RuO$_2$/CCO, RuO$_2$/CFO, RuO$_2$/CNO, RuO$_2$, and RuO$_2$/CMO catalysts. c) Comparison of bifunctional activities for RuO$_2$/CCO, RuO$_2$/CFO, RuO$_2$/CNO, and RuO$_2$/CMO catalysts. d) ORR LSV polarization curves for CMO, RuO$_2$, commercial Pt/C, and RuO$_2$/CMO catalysts. e) Corresponding Tafel slope of ORR curves. f) ORR LSV curves of first and 2000 cycles for RuO$_2$/CMO catalyst. g) OER LSV polarization curves for CMO, RuO$_2$, commercial IrO$_2$, and RuO$_2$/CMO catalysts. h) Corresponding Tafel slope of OER curves. i) OER stability at 10 mA cm$^{-2}$ for RuO$_2$/CMO catalyst. j) Comparison of bifunctional activities for CMO, RuO$_2$, commercial Pt/C-IrO$_2$, and RuO$_2$/CMO catalyst. k) Comparison of bifunctional activities of this work with reported catalysts.

(Supporting Information). To confirm the bifunctional activity, OER electrocatalytic activity for these composite catalysts was collected from LSV curves in Figure 2b. RuO$_2$/CMO catalyst only required a lower overpotential of 310 mV at 10 mA cm$^{-2}$ than that of 350, 390, and 370 mV for RuO$_2$/CCO, RuO$_2$/CFO, and RuO$_2$/CNO, respectively. Otherwise, as shown in Figure S8 (Supporting Information), the Tafel slope of the RuO$_2$/CMO cat-

alyst was calculated as 86 mV dec$^{-1}$, which outperformed that of other composite catalysts, including RuO$_2$/CCO (107 mV dec$^{-1}$), RuO$_2$/CFO (110 mV dec$^{-1}$) and RuO$_2$/CNO (114 mV dec$^{-1}$), revealing its lower overpotential at higher current density and faster OER kinetic rate. To confirm the advantage of supported catalysts, we further compared the ORR and OER activity of composite catalysts with Co-based spinel oxides (Figures S9 and

S10, Supporting Information) and $RuO_2$. The potential for ORR at $-2$ mA cm$^{-2}$ and OER at 10 mA cm$^{-2}$ were summarized in Figure 2c. The ORR/OER activity of composite catalysts is superior to their corresponding single-phase catalysts, which is mainly attributed to the synergistic effect between the $RuO_2$ and Co-based spinel oxides. In addition, the bifunctional activity of composite catalysts follows the sequence $RuO_2/CMO > RuO_2/CCO > RuO_2/CNO > RuO_2/CFO$, which means that CMO spinel oxides may be the optimum supports for $RuO_2$ to boost ORR and OER activities.

To further explore the synergistic effect in $RuO_2/CMO$, we select $RuO_2$ and CMO as counterparts for analysis, while commercial Pt/C and commercial $IrO_2$ have been taken as comparisons. Figure 2d displays the typical ORR polarization curves collected from LSV curves. $RuO_2/CMO$ delivered higher half-potential and diffusion-limited current densities than CMO ($E_{1/2} = 0.76$ V, $J_1 = 4.6$ mA cm$^{-2}$) and pure $RuO_2$ ($E_{1/2} = 0.53$ V, $J_1 = 4.2$ mA cm$^{-2}$), even approaching the benchmark of Pt/C ($E_{1/2} = 0.82$ V, $J_1 = 6.1$ mA cm$^{-2}$). In addition, $RuO_2/CMO$ performs the lowest Tafel slope compared with CMO (91 mV dec$^{-1}$), $RuO_2$ (157 mV dec$^{-1}$), and Pt/C (114 mV dec$^{-1}$), revealing the existence of a synergistic effect between $RuO_2$ and CMO to improve the ORR kinetics rate (Figure 2e). Moreover, $RuO_2/CMO$ exhibited more active sites for oxygen adsorption than CMO and $RuO_2$ from CV curves in Figure S11 (Supporting Information). To investigate ORR mechanism, a rotating ring-disc electrode (RRDE) technology was adopted to collect the $H_2O_2$ yield rate to calculate the electron transfer number (n) through the Koutecky–Levich (K–L) equation within the potential range of 0.2–0.8 V.[29] The electron transfer number of the $RuO_2/CMO$ catalyst was calculated to be ≈3.83, which is close to the Pt/C (n = 3.93), revealing a four-electron pathway for ORR (Figure S12, Supporting Information).[30] Furthermore, ORR stability of $RuO_2/CMO$ was evaluated by accelerated tests in 0.1 M KOH within $-0.7–0.2$ V (vs Hg/HgO). As shown in Figure 2f, $RuO_2/CMO$ catalysts perform a negligible decay of half-wave potential and limiting current density after 2000 cycles, which is far superior to CMO, indicating outstanding ORR durability after introducing $RuO_2$ on the CMO surface. In addition, benchmark Pt/C shows a tremendous decrease in limiting current density after 2000 CV cycles (Figure S13, Supporting Information).

The OER electrocatalytic activity of $RuO_2/CMO$ and counterparts was also evaluated using the same electrolytic device. As shown in Figure 2g, $RuO_2/CMO$ performs a 100 mV decrease in overpotential at 10 mA cm$^{-2}$ compared to CMO and $RuO_2$, and also shows lower overpotential than commercial $IrO_2$ (440 mV). Otherwise, the Tafel slope of $RuO_2/CMO$ catalyst was calculated as 86 mV dec$^{-1}$, outperforming contrastive catalysts, e.g., CMO (117 mV dec$^{-1}$), $RuO_2$ (131 mV dec$^{-1}$) and commercial $IrO_2$ (136 mV dec$^{-1}$), revealing its lower overpotential at higher current density and faster OER kinetic rate (Figure 2h). To explain the significant improvement in activity, we further tested the electrochemical surface area (ECSA) of the catalyst by measuring double-layer capacitance ($C_{dl}$).[31] As shown in Figure S14 (Supporting Information), $RuO_2/CMO$ achieves the $C_{dl}$ value of 15.2 mF cm$^{-2}$, which is 7.6 and 2.8 times that of $RuO_2$ and CMO, implying the combination of $RuO_2$ and CMO can enhance their actual active sites. The enhancement of the catalytic site is mainly related to the interface interaction, which can improve the OH$^-$

adsorption capacity. Furthermore, we compared the specific activity and mass activity of $RuO_2/CMO$, $RuO_2$, and CMO catalysts at the potential of 1.6 V versus RHE. As shown in Figure S15 (Supporting Information), $RuO_2/CMO$ performs higher specific activity than $RuO_2$ and CMO, and the mass activity of $RuO_2/CMO$ is 17.45 times that of $RuO_2$ based on Ru mass, revealing the superiority of hetero-interface. Besides, the OER stability was further conducted through chronopotentiometry measurement at 10 mA cm$^{-2}$. As shown in Figure 2i, $RuO_2/CMO$ delivered a low increase of 30 mV in overpotential after 20 h, which was lower than that of 170 mV for commercial $IrO_2$. Further, an accelerated OER durability test was conducted within the potential range of 1.1–1.7 V versus RHE in Figure S16 (Supporting Information). $RuO_2/CMO$ performs a slight decay of only 30 mV after 2000 cycles, while the charge transfer impedance was just slightly decreased, implying the excellent OER durability of $RuO_2/CMO$. We further obtained the relevant information on $RuO_2/CMO$ catalysts after the OER stability test. The concentration of Co, Mn, and Ru in electrolytes after the OER stability test of 10 h at 10 mA cm$^{-2}$ were just 9.29, 8.25, and 12.14 ppb for $RuO_2/CMO$ catalysts. In addition, the binding energy of Ru $3d_{5/2}$, Co 2p, and Mn 2p after the OER test was well maintained compared with that before the OER test (Figure S17, Supporting Information). The above result indicates that the structure of $RuO_2/CMO$ catalysts is well maintained during the OER process.

The overall bifunctional electrochemically activity of $RuO_2/CMO$ was evaluated through the potential difference ($\Delta E$) between the half-wave potential ($E_{1/2}$) of ORR and the potential of OER at 10 mA cm$^{-2}$ ($E_{j = 10 mA cm-2}$). As shown in Figure 2j, $RuO_2/CMO$ delivered the lowest $\Delta E$ of 0.74 V, which is much smaller than CMO (0.88 V) and $RuO_2$ (1.13 V), especially lower than the commercial catalyst (Pt/C-$IrO_2$) with 0.85 V (Figure S18, Supporting Information), confirming the excellent bifunctional activity of $RuO_2/CMO$. Therefore, growing $RuO_2$ on Mn-doped $Co_3O_4$ supports can drastically enhance the ORR and OER activity to form a profitable bifunctional catalyst. Significantly, we compared the $\Delta E$ value of recently reported Ru-based and spinel-based catalysts in Figure 2k (Detailed information in Table S2, Supporting Information). $RuO_2/CMO$ achieves a lower $\Delta E$ value compared with recently reported works, strongly confirming the super bifunctional catalytic activity of $RuO_2/CMO$ again. Compared to CMO and $RuO_2$, its composite catalyst exhibits a significant synergistic effect in improving ORR and OER activities. Therefore, we further explore the synergistic mechanism for offering a desirable direction in designing bifunctional oxygen catalysts.

X-ray photoelectron spectroscopy (XPS) technology was first conducted to identify ORR and OER active sites by correlating the binding energy of active sites with catalytic activities. For the pure CCO, the Co $2p_{3/2}$ spectrum can deconvolute into $Co^{3+}$ and $Co^{2+}$ peaks that are located at 780.0 and 781.5 eV, respectively (**Figure 3a**).[32] Compared with the CCO, the $Co^{3+}$ and $Co^{2+}$ peaks of CMO presented positive transitions, which indicates that Mn-doping can regulate the electronic structure of CCO support.[33] After introducing $RuO_2$ nanorods, the $Co^{3+}$ peak of $RuO_2/CMO$ is negatively shifted to low binding energy.[16] Compared to $RuO_2/CCO$, $RuO_2/CMO$ shows a positive shift of the $Co^{3+}$ peak owing to the regulation of the electronic structure of spinel oxide by Mn-doping. Differently, the $Co^{3+}$ peak
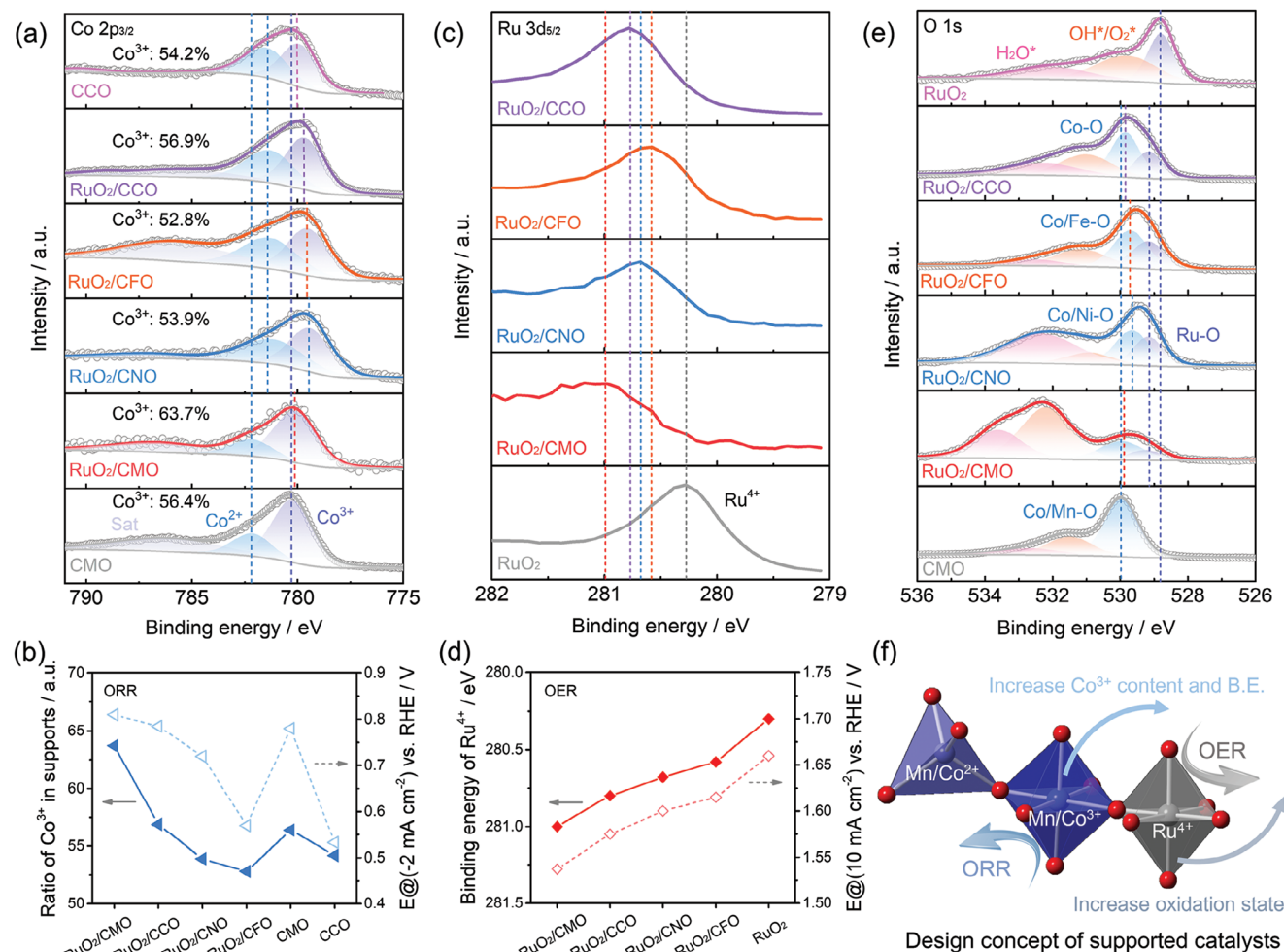
**ADVANCED**
**SCIENCE NEWS**
www.advancedsciencenews.com

**ADVANCED**
**FUNCTIONAL**
**MATERIALS**
www.afm-journal.de

**Figure 3.** Identifying ORR and OER active sites. a) Co $2p_{3/2}$ for CMO, CCO, RuO$_2$/CCO, RuO$_2$/CFO, RuO$_2$/CNO, and RuO$_2$/CMO catalysts. b) Comparison of the ratio of Co$^{3+}$ at the spinel supports and the ORR potential of CMO, CCO, RuO$_2$/CCO, RuO$_2$/CFO, RuO$_2$/CNO, and RuO$_2$/CMO catalysts at −2 mA cm$^{-2}$. c) Ru $3d_{5/2}$ for RuO$_2$, RuO$_2$/CCO, RuO$_2$/CFO, RuO$_2$/CNO, and RuO$_2$/CMO catalysts. d) Comparison of the binding energy of Ru$^{4+}$ and the OER potential of RuO$_2$, RuO$_2$/CCO, RuO$_2$/CFO, RuO$_2$/CNO, and RuO$_2$/CMO catalysts at 10 mA cm$^{-2}$. e) O 1s for CMO, RuO$_2$, RuO$_2$/CCO, RuO$_2$/CFO, RuO$_2$/CNO, and RuO$_2$/CMO catalysts. f) Schematic illustration of the design concept of RuO$_2$-based supported catalysts.

of RuO$_2$/CFO and RuO$_2$/CNO was negatively shifted compared with RuO$_2$/CCO. The different Co$^{3+}$ binding energy may greatly affect ORR activities. We have previously tested the ORR activity of these composite catalysts. Compared to RuO$_2$/CCO, the ORR activity of Ru/CMO is increased, while the activity of Ru/CFO and Ru/CNO is significantly reduced. Therefore, we believe that the electronic structure of Co$^{3+}$ has a significant impact on ORR activities. Previous literature on spinel oxide has also indicated that the trivalent ions at the B-site provide the main ORR active sites.[34] The content of Co$^{3+}$ active sites may be an important indicator for ORR activities. The doped Ni, Fe, and Mn perform divalent and trivalent (Figure S19, Supporting Information), which may induce different Co$^{3+}$ content in Co-based spinel oxide. The percentage of Co$^{3+}$ phase is fitted to 63.7% for RuO$_2$/CMO catalyst, 54.2% for CCO, 56.4% for CMO, 56.9% for RuO$_2$/CCO, 52.8% for RuO$_2$/CFO, and 53.9% for RuO$_2$/CNO. We found a correlation between the content of Co$^{3+}$ and ORR activity as shown in Figure 3b, which is well consistent with recent studies for increasing the content of Co$^{3+}$ in octahedron sites of Co$_3$O$_4$ can

enhance the ORR catalytic activity.[35] Therefore, the consistent linear relationship indicates that Co$^{3+}$ serves as the main ORR active site in the composite catalyst, RuO$_2$/Co-based spinel oxide, while increasing the binding energy and content of Co$^{3+}$ is beneficial to ORR activities.

Generally, OER catalytic activities of metal oxide are governed by the electronic structure of metal-oxygen bonds. We further detect the XPS spectra of Ru $3d_{5/2}$ for all composite catalysts. As shown in Figure 3c, RuO$_2$ performs one peak of Ru$^{4+}$ located at 280.3 eV, which is consistent with previous studies.[36] After integrating RuO$_2$ onto the surface of Co-based spinel oxide, the position of Ru$^{4+}$ peak shifts toward high binding energy for composite catalysts, which follows the sequence of RuO$_2$/CMO (281.0 eV) > RuO$_2$/CCO (280.8 eV) > RuO$_2$/CNO (280.68 eV) > RuO$_2$/CFO (280.58 eV). The binding energy of Ru$3d_{5/2}$ is highly related to the oxidation state of Ru in RuO$_2$, which is a key descriptor of OER activities.[37] We compared the oxidation state of Ru in composite catalysts with OER activities and found a positive correlation (Figure 3d). The correlation means that Ru atoms

**ADVANCED
SCIENCE NEWS**

www.advancedsciencenews.com

**ADVANCED
FUNCTIONAL
MATERIALS**

www.afm-journal.de

in the loaded $RuO_2$ provide the main OER catalytic site for the composite catalysts. Besides, regulating the electronic structure of Co-based spinel oxide supports is beneficial for optimizing the oxidation state of Ru in the loaded $RuO_2$, thus optimizing the OER catalytic activity.

$RuO_2$/CMO achieves a negative shift of $Co^{3+}$ compared to CMO and a positive shift of $Ru^{4+}$ compared to $RuO_2$, which means the charge rearrangement between $Co^{3+}$ and $Ru^{4+}$ in the hetero-interface through O atoms bridge. We further detect the XPS spectra of O 1s for all composite catalysts (Figure 3e). The O 1s spectrum of $RuO_2$ and CMO can deconvolute into three species, including lattice oxygen (metal—O bond), $^*OH$, and adsorbed $^*H_2O$.[38] As for composite catalysts, two phases can induce two types of lattice oxygen. Therefore, the O 1s spectrum of composite catalysts can fitted into four species, including Ru-O, Co/Fe/Ni/Mn-O, $^*OH$, and adsorbed $^*H_2O$. Significantly, all composite catalysts show the position of Ru—O peak shifts toward high binding energy compared to $RuO_2$ and the position of Co/Fe/Ni/Mn—O peak shifts toward low binding energy compared to CMO. This charge rearrangement causes electrons to flow from $RuO_2$ to Co-based spinel oxide supports, resulting in enhanced lattice oxygen bonds in the $RuO_2$ and weakened lattice oxygen bonds in Co-based spinel oxide supports. In addition, $RuO_2$/CMO exhibited higher content of $^*OH$ than other catalysts owing to the high oxidation state $Ru^{4+}$ in favoring the adsorption of $^*OH$, indicating the Ru site can serve as an adsorption site for $OH^-$ and $O_2$ to trigger OER and ORR, respectively. However, too strong an adsorption ability will inevitably lead to difficulties in the desorption of $OH^-$ and $O_2$, therefore the CMO supports may play a role in accelerating the desorption of $OH^-$ and $O_2$ species to trigger the synergistic effect with $RuO_2$.[39] These results prove the intrinsic relation between electrocatalytic activities and active sites for $RuO_2$-supported Co-based spinel oxides. Therefore, as shown in Figure 3f, increasing the content and binding energy of $Co^{3+}$ and enhancing the oxidation state of $Ru^{4+}$ is an efficient strategy to promote ORR and OER activities for $RuO_2$/Co-based spinel oxide composite catalysts.

To further explore the synergistic mechanism of $Co^{3+}$ and $Ru^{4+}$, we conducted operando electrochemical impedance spectroscopy (EIS) to explore the potential-dependent reaction behavior under a three-electrode system. As presented in Figure S20 (Supporting Information), the EIS plot of OER was collected from 0.3 to 0.8 V versus Hg/HgO reference. We found that the charge transfer impedance decreases with the increase of potential. To obtain more information, the corresponding bode plot was acquired from EIS results (Figure S21, Supporting Information). As reported, the peak phase and peak frequency from the bode plot of OER are the key indicators to reflect the number of involved electrons and charge transfer rate, respectively.[40] As exhibited in **Figure 4a**, the peak frequency of $RuO_2$ is much higher than CMO supports after the onset potential, confirming a faster electron transfer rate from the intermediate species to Ru sites than Co/Mn sites during OER. These results further prove that the Ru sites in $RuO_2$/CMO provide the main OER catalytic site. Differently, the peak phase of CMO supports is lower than $RuO_2$ after the onset potential, which means that the CMO shows easier oxygen desorption ability than $RuO_2$. In particular, $RuO_2$/CMO achieves the lowest peak phase compared with pure $RuO_2$ and CMO, indicating the incorporation

of $RuO_2$ and CMO can promote oxygen desorption. The typical bode plot at 0.75 V versus Hg/HgO (non-iR corrected)) is presented in Figure 4b. $RuO_2$/CMO, $RuO_2$, and CMO achieve relaxation times of 33.5, 21.3, and 69.1 ms, respectively. Generally, the relaxation time shows a negative relationship with the charge transfer rate in the interface of catalysts and electrolytes.[41] In addition, the peak phase follows the sequence of $RuO_2$/CMO (12.3°) > CMO (19.0°) > $RuO_2$ (36.5°), which indicates the number of involved electrons during OER at this potential. Therefore, as for $RuO_2$/CMO, $RuO_2$ is involved in the main charge transfer steps, while CMO provides the desorption site for oxygen during the OER process.

In addition, the EIS collected from 0 to −0.4 V versus Hg/HgO and the corresponding bode plot during the ORR process are also displayed in Figures S22 and S23 (Supporting Information), respectively. ORR involves two processes of mass-transport and charge transfer in the mixed diffusion-controlled region, which can be identified at the region of low-frequency ($10^0$–$10^1$ Hz) and low-frequency ($10^1$–$10^2$ Hz) in bode plots.[7b] Here we extract the phase value at the same frequency of different potentials to probe the mechanism, in which the frequency of 0.1 and 3 Hz represent the mass-transfer and kinetic region, respectively. As depicted in Figure 4c, $RuO_2$/CMO exhibited similar evolution trends with CMO for the mass transport and charge transfer behavior. Especially, the phase value of $RuO_2$/CMO and CMO was lower than that of $RuO_2$ in the mixed region, indicating that the CMO support in $RuO_2$/CMO performs the charge transfer process of ORR. In addition, $RuO_2$/CMO shows a higher phase value than CMO in the mixed region for the mass transport behavior, indicating that the integration of $RuO_2$ on the CMO surface can strengthen the mass transport ability. Therefore, $RuO_2$ and CMO support in $RuO_2$/CMO provides the site for oxygen adsorption and adsorbent evolution, respectively. In the mixed region, we further collect the bode plot at the same current density of 4 mA cm$^{-2}$ for the three catalysts (Figure 4d). For the charge transfer, the low phase sequence means a faster charge transfer rate. $RuO_2$/CMO and CMO achieve lower phase values than $RuO_2$, which strongly suggests that CMO offers the catalytic site for the kinetic step. Besides, for the mass transport, the phase sequence of $RuO_2$ is higher than CMO supports, further confirming that $RuO_2$ promotes mass adsorption under the same current density during the ORR process.

We further conducted density functional theory (DFT) calculation to prove the above reaction mechanism. The crystal plane of (111) and (110) is selected as active faces for CMO and $RuO_2$ to conduct adsorbent species evolution (Figure S24, Supporting Information). Specifically, we also build the heterostructure between CMO and $RuO_2$ to obtain the crystal configuration of $RuO_2$/CMO. First, the charge density difference at the heterostructure of CMO and $RuO_2$ is calculated as shown in Figure 4e. It can be observed that the charge at the heterointerface is biased toward CMO and away from $RuO_2$, which is consistent with the previous XPS results for transferring electrons from $RuO_2$ to CMO supports. The electron transfer number is estimated as 2.7 eV through Bader calculation.[42] Generally, the interface electronic interaction will lead to strong catalyst-support interaction, thus inducing the overflow of adsorbed species at the interface, such as oxygen overflow,[3a,43] which may be the origin of the synergistic effect between $RuO_2$ and CMO supports.

**ADVANCED
SCIENCE NEWS**

www.advancedsciencenews.com

**ADVANCED
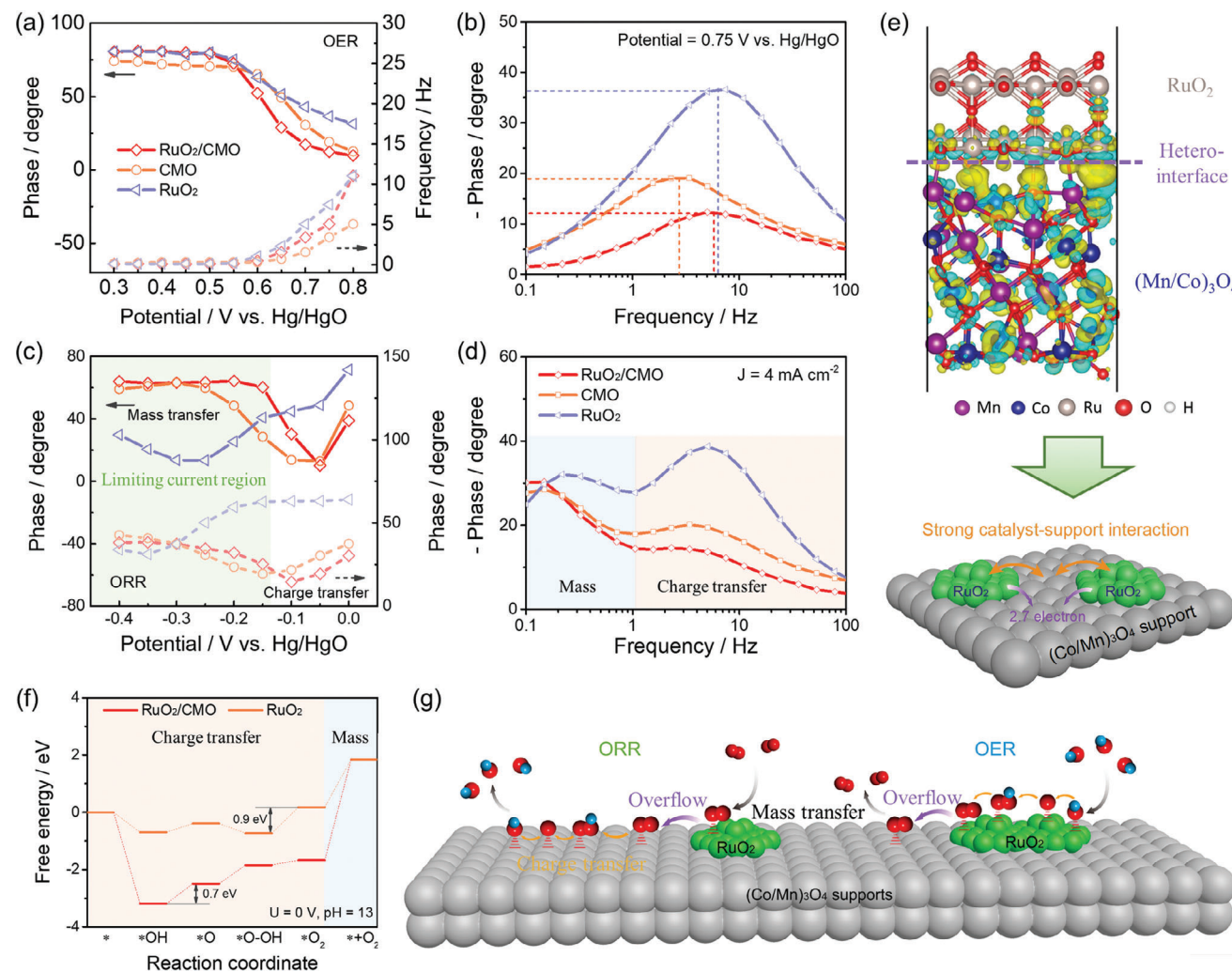FUNCTIONAL
MATERIALS**

www.afm-journal.de

**Figure 4.** ORR and OER mechanism of RuO$_2$-based supported catalysts. EIS-bode plots of OER: a) comparison of phase value and Frequency of various catalysts at 0.3–0.8 V versus Hg/HgO and b) frequency-phase curves of various catalysts at 0.75 V versus Hg/HgO EIS-bode plots of ORR: c) comparison of phase value and Frequency at the potential of −0.4–0.0 V versus Hg/HgO and d) frequency–phase curves at j = 4 mA cm$^{−2}$ for CMO, RuO$_2$, and RuO$_2$/CMO catalysts. e) Charge density difference of RuO$_2$/CMO. Isosurface level was set at 0.03 e Å$^{−3}$. Charge accumulation and depletion were presented with the yellow and cyan areas, respectively. f) Calculated free energy diagrams for RuO$_2$ and RuO$_2$/CMO. g) ORR and OER mechanism for RuO$_2$/CMO supported catalyst.

Furthermore, the adsorption ability of different oxygen intermediate species is obtained by calculating the Gibbs free energy.[44] The single-site pathway is unsuitable for adsorbing intermediate species owing to the extreme overpotential (Figures S25 and S26, Supporting Information). We further consider the adsorption configuration in a dual-site pathway (Figure S27, Supporting Information). OER can be divided into two processes, in which the kinetic step involves electron transfer and the diffusion step points to oxygen desorption.[45] As illustrated in Figure 4f, RuO$_2$/CMO performs a low kinetic overpotential of 0.24 eV, which outperforms that of 0.44 eV for RuO$_2$. However, both RuO$_2$/CMO and RuO$_2$ demonstrate a high barrier for oxygen desorption owing to the strong Ru-O covalence. CMO supports perform an electron-rich characteristic owing to the strong interface interaction, which is beneficial for oxygen overflow to its surface. Similarly, as for the ORR process, RuO$_2$/CMO performs

a high kinetic overpotential of 3.65 eV on Ru sites for *OH desorption. In contrast, CMO supports provide the main catalytic sites for ORR owing to the low overpotential of *OH desorption on CMO (Figure S28, Supporting Information). Especially, the co-adsorption of oxygen intermediate species, OH*, O*, and OOH*, on Co/Mn sites performs the optimal reaction pathway, thus Co/Mn dual-atoms involve the main ORR process. DFT calculation is well consistent with the results of XPS analysis and operando EIS. According above discussion, we propose the bifunctional catalytic mechanism of RuO$_2$/CMO composite catalysts in Figure 4g. For the ORR process, the kinetic step of ORR mainly occurs on the CMO support, while the first step for the oxygen adsorption occurs on RuO$_2$ considering the strong adsorption ability toward oxygen. In the OER process, RuO$_2$ conducts the kinetic step and CMO supports facilitate the oxygen desorption to alleviate the strong oxygen adsorption ability of RuO$_2$.

**ADVANCED
SCIENCE NEWS**

www.advancedsciencenews.com

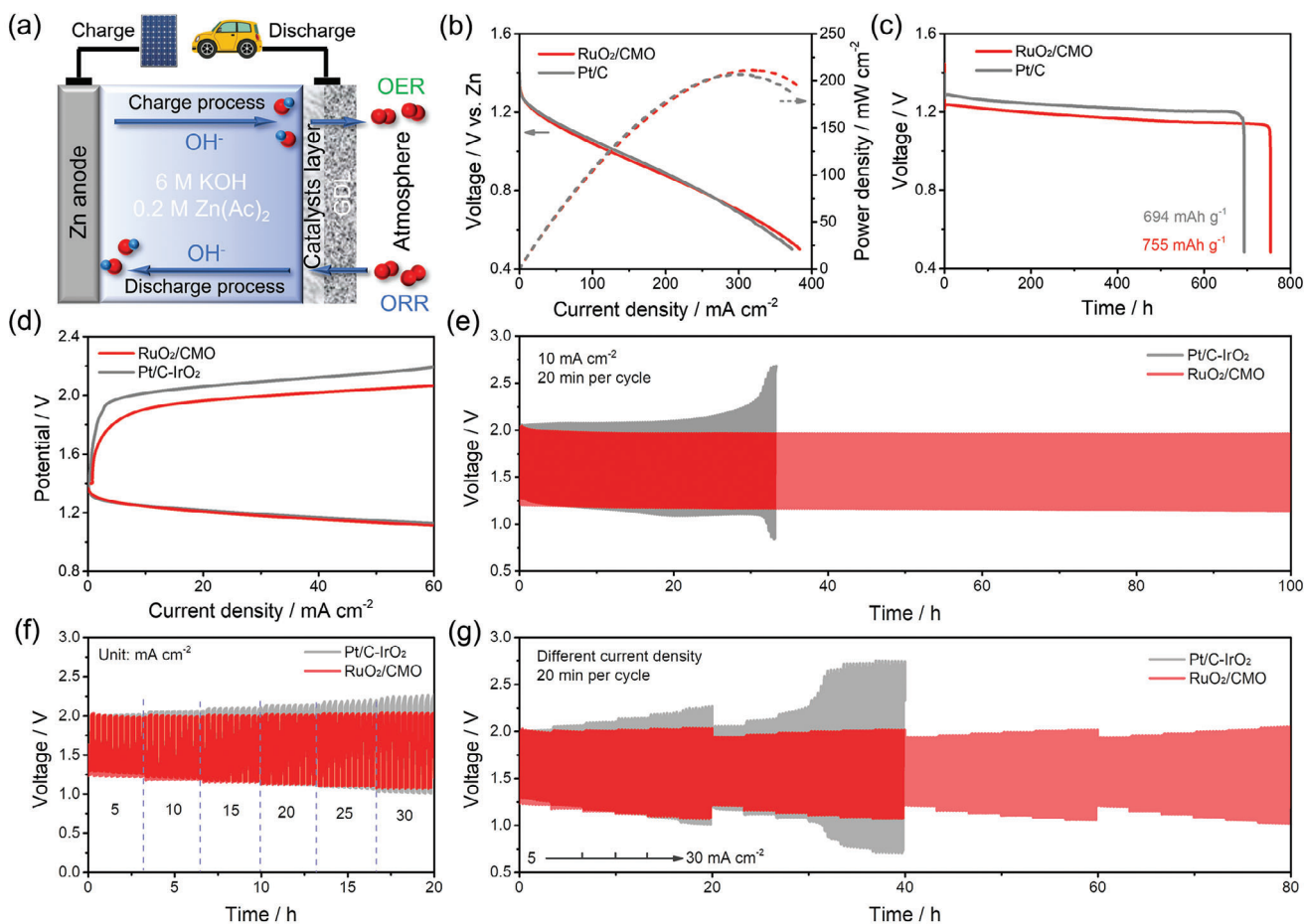**ADVANCED
FUNCTIONAL
MATERIALS**

www.afm-journal.de

**Figure 5.** Cyclic behaviors of rechargeable zinc–air batteries. a) Structure illustration of home-made Zn–air batteries. b) Power density and c) discharge capacities at 10 mA cm$^{-2}$ of RuO$_2$/CMO and Pt/C catalysts. d) Charging/discharging polarization curves of RuO$_2$/CMO and Pt-IrO$_2$ catalysts. e) Cycling performance of RuO$_2$/CMO and Pt-IrO$_2$ catalysts at 10 mA cm$^{-2}$ with 20 min per cycle. f,g) Rating performance of RuO$_2$/CMO and Pt-IrO$_2$ catalysts.

During ORR and OER, oxygen overflow occurs at the heterointerface between RuO$_2$ and CMO supports to trigger the synergistic effect.

RuO$_2$/CMO performs excellent bifunctional ORR/OER activities, which can be further investigated by assembling Zn–air batteries, while commercial Pt/C-IrO$_2$ catalysts serve as a comparison. **Figure 5**a depicts the structure of homemade Zn–air batteries in this work. RuO$_2$/CMO catalyst performs a higher peak power density of 211 mW cm$^{-2}$ than that of 206 mW cm$^{-2}$ for benchmark Pt/C (Figure 5b). Especially, the discharge specific capacity of RuO$_2$/CMO at 10 mA cm$^{-2}$ reaches 755 mAh g$^{-1}$, based on the consumption of zinc anode (Figure S29, Supporting Information), exceeding the Pt/C-IrO$_2$ with 694 mAh g$^{-1}$ as inhibited in Figure 5c, revealing the potential of RuO$_2$/CMO to substitute Pt/C-IrO$_2$ in pristine Zn–air batteries.

Furthermore, the charge test was subsequently conducted to assess the discharge/charge overpotential of bifunctional catalysts. As exhibited in Figure 5d, RuO$_2$/CMO-assembled Zn–air batteries showed much lower charge potential than Pt/C-IrO$_2$ catalyst at a current density from 0 to 60 mA cm$^{-2}$, which is well consistent with OER results. Cycling and rating performance are key parameters for evaluating rechargeable Zn–air batteries.

The repeated discharge and charge cycle tests were performed by the galvanostatic measurement at 10 mA cm$^{-2}$. As shown in Figure 5e, RuO$_2$/CMO catalyst-based Zn–air batteries could maintain a stable lifespan of over 100 h without obvious polarization decay, which is ≈3 times longer than Pt/C-IrO$_2$. Meanwhile, the discharge/charge overpotential of RuO$_2$/CMO is significantly lower than that of Pt/C-IrO$_2$. The rating performance of bifunctional catalysts is further assessed by comparing the discharge-charge voltage profiles and stability at current densities ranging from 5 to 30 mA cm$^{-2}$. As illustrated in Figure 5f, the Zn–air battery assembled with RuO$_2$/CMO performs a slight increase in charge and discharge voltage platform when increasing current density. Significantly, the charging voltage of RuO$_2$/CMO is lower than Pt/C-IrO$_2$, especially at high current densities. RuO$_2$/CMO performs a lower voltage of 2.04 V at 30 mA cm$^{-2}$ than that of 2.26 V for Pt/C-IrO$_2$. To further confirm the stability of RuO$_2$/CMO in rechargeable Zn–air batteries, we repeat the rating test four times as shown in Figure 5g. After four rating tests in rechargeable Zn–air batteries, RuO$_2$/CMO catalysts showed only a slight increase in charge/discharge overpotential compared to the beginning, while Pt/C-IrO$_2$ performed death after the second rating test. The above cycling and rating

**ADVANCED
SCIENCE NEWS**

www.advancedsciencenews.com

**ADVANCED
FUNCTIONAL
MATERIALS**

www.afm-journal.de

performance of RuO$_2$/CMO catalysts reveals its potential commercial applications in rechargeable Zn–air batteries. The slight decrease of charge/discharge voltage gap at high current density may originated from the formation of dead zinc in the anode surface. In future work, we can consider using a 3D zinc anode to achieve better cycling performance of Zn–air batteries under high current density. Finally, we applied three homemade Zn–air batteries in series to lighten an LED screen (Figure S30, Supporting Information), revealing the potential application of the designed RuO$_2$/CMO catalyst in practical devices.

## 3. Conclusion

In conclusion, we designed a bifunctional catalyst via screening the optimum Co-based spinel oxide to supporting RuO$_2$ and found that RuO$_2$ nanorod supported on Mn-doped Co$_3$O$_4$, prepared through facile sol-gel method, achieves the lowest ORR/OER overpotential gap of 0.74 V in 0.1 M KOH, outperforming commercial Pt/C-IrO$_2$ benchmarks. Through XPS technology, we found that spinel oxide supports in composite catalysts provide the main ORR active site considering the positive correlation between the content of Co$^{3+}$ and ORR activity, and RuO$_2$ in composite catalysts involved in the main OER process considering the positive correlation between the oxidation state of Ru and OER activity. In addition, the synergistic effect between RuO$_2$ and CMO supports originated from the oxygen overflow to overcome the large barrier for oxygen desorption on RuO$_2$ during OER and oxygen adsorption on CMO supports during ORR. As a result, RuO$_2$/CMO assembled Zn–air batteries perform a high peak power density and specific capacity of 211 mW cm$^{-2}$ and 755 mAh g$^{-1}$, respectively, and even a long cycling life of over 100 h at 10 mA cm$^{-2}$. This work inspires explorations of novel oxide supports to design composite catalysts for next-generation green energy.

## Supporting Information

Supporting Information is available from the Wiley Online Library or from the author.

## Acknowledgements

## Conflict of Interest

The authors declare no conflict of interest.

## Data Availability Statement

The data that support the findings of this study are available from the corresponding author upon reasonable request.

## Keywords

[1] a) Y. Zhang, B. Chen, D. Q. Guan, M. G. Xu, R. Ran, M. Ni, W. Zhou, R. O'Hayre, Z. P. Shao, *Nature* **2021**, *591*, 246; b) M. Winter, B. Barnett, K. Xu, *Chem. Rev.* **2018**, *118*, 11433; c) X. H. Zou, Q. Lu, C. E. Wang, S. X. She, K. M. Liao, R. Ran, W. Zhou, L. An, Z. P. Shao, *J. Membr. Sci.* **2023**, *665*, 121112; d) X. Zou, M. Tang, Q. Lu, Y. Wang, Z. Shao, L. An, *Energy Environ. Sci.* **2024**, *17*, 386.

[2] a) M. C. Luo, Z. L. Zhao, Y. L. Zhang, Y. J. Sun, Y. Xing, F. Lv, Y. Yang, X. Zhang, S. Hwang, Y. N. Qin, J. Y. Ma, F. Lin, D. Su, G. Lu, S. J. Guo, *Nature* **2019**, *574*, 81; b) X. Zou, Q. Lu, K. Liao, Z. Shao, *Energy Storage Mater.* **2022**, *45*, 869; c) J. Li, H. Xue, N. Xu, X. Zhang, Y. Wang, R. He, H. Huang, J. Qiao, *Mater. Rep. Energy* **2022**, *2*, 100090.

[3] a) Z. P. Wang, J. H. Huang, L. Wang, Y. Y. Liu, W. H. Liu, S. L. Zhao, Z. Q. Liu, *Angew. Chem.-Int. Edit.* **2022**, *61*, 202114696; b) T. Tang, Z. Jiang, J. Deng, S. Niu, Z.-C. Yao, W.-J. Jiang, L.-J. Zhang, J.-S. Hu, *Nano Res.* **2022**, *15*, 10021.

[4] a) X. T. Wang, T. Ouyang, L. Wang, J. H. Zhong, Z. Q. Liu, *Angew. Chem.-Int. Edit.* **2020**, *59*, 6492; b) Y. Huang, J.-J. Wang, Y. Zou, L.-W. Jiang, X.-L. Liu, W.-J. Jiang, H. Liu, J.-S. Hu, *Chin. J. Catal* **2021**, *42*, 1395.

[5] C. Li, X. P. Han, F. Y. Cheng, Y. X. Hu, C. C. Chen, J. Chen, *Nat. Commun.* **2015**, *6*, 7345.

[6] T. P. Zhou, N. Zhang, C. Z. Wu, Y. Xie, *Energy Environ. Sci.* **2020**, *13*, 1132.

[7] a) H. B. Tao, J. M. Zhang, J. Z. Chen, L. P. Zhang, Y. H. Xu, J. G. G. Chen, B. Liu, *J. Am. Chem. Soc.* **2019**, *141*, 13803; b) Q. Lu, X. H. Zou, X. X. Wang, L. An, Z. P. Shao, Y. F. Bu, *Appl. Catal. B-Environ.* **2023**, *325*, 122323.

[8] a) P. Yu, L. Wang, F. F. Sun, Y. Xie, X. Liu, J. Y. Ma, X. W. Wang, C. G. Tian, J. H. Li, H. G. Fu, *Adv. Mater.* **2019**, *31*, 1901666; b) J. Wang, W. Liu, G. Luo, Z. J. Li, C. Zhao, H. R. Zhang, M. Z. Zhu, Q. Xu, X. Q. Wang, C. M. Zhao, Y. T. Qu, Z. K. Yang, T. Yao, Y. F. Li, Y. Lin, Y. Wu, Y. D. Li, *Energy Environ. Sci.* **2018**, *11*, 3375; c) Q. Lu, X. Zou, Y. Bu, K. Liao, W. Zhou, Z. Shao, *Small* **2022**, *18*, 2105604.

[9] Z. M. Cui, G. T. Fu, Y. T. Li, J. B. Goodenough, *Angew. Chem.-Int. Edit.* **2017**, *56*, 9901.

[10] Q. Wang, L. Shang, R. Shi, X. Zhang, Y. F. Zhao, G. I. N. Waterhouse, L. Z. Wu, C. H. Tung, T. R. Zhang, *Adv. Energy Mater.* **2017**, *7*, 1700467.

[11] Z. H. Wu, Z. Wang, P. Xiong, G. H. Li, T. L. Qiu, W. B. Gong, F. F. Zhao, C. L. Li, Q. W. Li, G. X. Wang, F. X. Geng, *Nano Lett.* **2020**, *20*, 2892.

[12] a) Q. Lu, X. Zou, Y. Bu, L. An, Y. Wang, Z. Shao, *Next Energy* **2023**, *1*, 100025; b) X. F. Yang, F. B. Wang, Z. X. Jing, M. Chen, B. Wang, L. Wang, G. M. Qu, Y. Y. Kong, L. Q. Xu, *Small* **2023**, *19*, 2301985.

[13] a) C. H. Zhou, X. Chen, S. Liu, Y. Han, H. B. Meng, Q. Y. Jiang, S. M. Zhao, F. Wei, J. Sun, T. Tan, R. F. Zhang, *J. Am. Chem. Soc.* **2022**, *144*, 2694; b) Q. Lu, Y. N. Guo, P. Mao, K. M. Liao, X. H. Zou, J. Dai, P. Tan, R. Ran, W. Zhou, M. Ni, Z. P. Shao, *Energy Storage Mater.* **2020**, *32*, 20; c) H. Sun, H. Xu, H. Kim, Z. Shao, W. Jung, *InfoMat* **2024**, *6*, 12494.

[14] a) J. Y. Zhang, J. S. Lian, Q. Jiang, G. Y. Wang, *Chem. Eng. J.* **2022**, *439*, 135634; b) H. S. Wang, H. D. Abruña, *Appl. Catal. B-Environ* **2020**, *277*, 119149.

**ADVANCED
SCIENCE NEWS**

www.advancedsciencenews.com

**ADVANCED
FUNCTIONAL
MATERIALS**

www.afm-journal.de

[15] C. H. Zhou, S. M. Zhao, H. B. Meng, Y. Han, Q. Y. Jiang, B. S. Wang, X. F. Shi, W. S. Zhang, L. Zhang, R. F. Zhang, *Nano Lett.* **2021**, *21*, 9633.

[16] Y. X. Gao, D. B. Zheng, Q. C. Li, W. P. Xiao, T. Y. Ma, Y. L. Fu, Z. X. Wu, L. Wang, *Adv. Funct. Mater.* **2022**, *32*, 2203206.

[17] Y. Qiu, Y. F. Rao, Y. N. Zheng, H. Hu, W. H. Zhang, X. H. Guo, *InfoMat* **2022**, *4*, 12326.

[18] a) Q. Lu, X. H. Zou, Y. F. Bu, Z. P. Shao, *Energy Storage Mater.* **2023**, *55*, 166; b) T. Tang, W. J. Jiang, X. Z. Liu, J. Deng, S. Niu, B. Wang, S. F. Jin, Q. Zhang, L. Gu, J. S. Hu, L. J. Wan, *J. Am. Chem. Soc.* **2020**, *142*, 7116.

[19] X. J. Zhuang, Y. T. Zhou, Z. Q. Jiang, X. Z. Yao, X. Y. Yu, *J. Mater. Chem. A* **2021**, *9*, 26669.

[20] P. Gayen, S. Saha, K. Bhattacharyya, V. K. Ramani, *ACS Catal.* **2020**, *10*, 7734.

[21] J. Béjar, F. Espinosa-Magaña, M. Guerra-Balcázar, J. Ledesma-García, L. Álvarez-Contreras, N. Arjona, L. G. Arriaga, *ACS Appl. Mater. Interfaces* **2020**, *12*, 53760.

[22] S. Kumar, A. Tahira, A. L. Bhatti, M. A. Bhatti, Z. A. Ujjan, U. Aftab, S. Kumar, A. A. Al-Kahtani, A. Nafady, E. Dawi, M. Emo, B. Vigolo, A. Infantes-Molina, Z. H. Ibupoto, *J. Energy Storage* **2024**, *77*, 109994.

[23] H. Yu, H. Fan, X. Wu, H. Wang, Z. Luo, H. Tan, B. Yadian, Y. Huang, Q. Yan, *Energy Storage Mater.* **2016**, *4*, 145.

[24] P. Patta, Y. Y. Chen, M. Natesan, C. L. Sung, C. C. Yang, C. H. Wang, T. Fujigaya, Y. H. Chang, *ACS Catal.* **2023**, *13*, 13434.

[25] X. Y. Wang, Y. Liu, T. H. Zhang, Y. J. Luo, Z. X. Lan, K. Zhang, J. C. Zuo, L. L. Jiang, R. H. Wang, *ACS Catal.* **2017**, *7*, 1626.

[26] Y. Wang, R. Yang, Y. J. Ding, B. Zhang, H. Li, B. Bai, M. R. Li, Y. Cui, J. P. Xiao, Z. S. Wu, *Nat. Commun.* **2023**, *14*, 1412.

[27] X. M. Ge, Y. Y. Liu, F. W. T. Goh, T. S. A. Hor, Y. Zong, P. Xiao, Z. Zhang, S. H. Lim, B. Li, X. Wang, Z. L. Liu, *ACS Appl. Mater. Interfaces* **2014**, *6*, 12684.

[28] K. E. Gregorczyk, Y. Liu, J. P. Sullivan, G. W. Rubloff, *ACS Nano* **2013**, *7*, 6354.

[29] a) Q. Lu, J. Yu, X. H. Zou, K. M. Liao, P. Tan, W. Zhou, M. Ni, Z. P. Shao, *Adv. Funct. Mater.* **2019**, *29*, 1904481; b) J. Wu, Y. Han, Y. Bai, X. Wang, Y. Zhou, W. Zhu, T. He, Y. Wang, H. Huang, Y. Liu, Z. Kang, *Adv. Funct. Mater.* **2022**, *32*, 2203647.

[30] J. Wu, M. Hou, Z. Chen, W. Hao, X. Pan, H. Yang, W. Cen, Y. Liu, H. Huang, P. W. Menezes, Z. Kang, *Adv. Mater.* **2022**, *34*, 2202995.

[31] Y. W. Dai, J. Yu, J. Wang, Z. P. Shao, D. Q. Guan, Y. C. Huang, M. Ni, *Adv. Funct. Mater.* **2022**, *32*, 2111989.

[32] N. N. Xu, J. A. Wilson, Y. D. Wang, T. S. Su, Y. N. Wei, J. L. Qiao, X. D. Zhou, Y. X. Zhang, S. H. Sun, *Appl. Catal. B-Environ.* **2020**, *272*, 118953.

[33] C. Qin, B. Wang, Y. D. Wang, *Sens. Actuator B-Chem.* **2022**, *351*, 130943.

[34] Z. P. Wang, P. Y. Wu, X. B. Zou, S. Wang, L. Du, T. Ouyang, Z. Q. Liu, *Adv. Funct. Mater.* **2023**, *33*, 2214275.

[35] a) X. Han, G. He, Y. He, J. Zhang, X. Zheng, L. Li, C. Zhong, W. Hu, Y. Deng, T. Y. Ma, *Adv. Energy Mater.* **2018**, *8*, 1702222; b) Z. Liu, G. Wang, X. Zhu, Y. Wang, Y. Zou, S. Zang, S. Wang, *Angew. Chem.-Int. Edit.* **2020**, *59*, 4736.

[36] Z. P. Shi, J. Li, Y. B. Wang, S. W. Liu, J. B. Zhu, J. H. Yang, X. Wang, J. Ni, Z. Jiang, L. J. Zhang, Y. Wang, C. P. Liu, W. Xing, J. J. Ge, *Nat. Commun.* **2023**, *14*, 843.

[37] K. X. Wang, Y. L. Wang, B. Yang, Z. J. Li, X. T. Qin, Q. H. Zhang, L. C. Lei, M. Qiu, G. Wu, Y. Hou, *Energy Environ. Sci.* **2022**, *15*, 2356.

[38] A. Pendashteh, J. Palma, M. Anderson, R. Marcilla, *Appl. Catal. B-Environ.* **2017**, *201*, 241.

[39] K. X. Zhang, R. Q. Zou, *Small* **2021**, *17*, 2100129.

[40] L. M. Deng, S. Y. Liu, D. Liu, Y. M. Chang, L. L. Li, C. S. Li, Y. Sun, F. Hu, H. Y. Chen, H. Pan, S. J. Peng, *Small* **2023**, *19*, 2302238.

[41] a) Y. Du, D. P. Liu, T. Z. Li, Y. D. Yan, Y. Liang, S. C. Yan, Z. G. Zou, *Appl. Catal. B-Environ.* **2022**, *306*, 121146; b) W. Y. Gou, Z. M. Xia, X. H. Tan, Q. Y. Xue, F. Ye, S. Dai, M. K. Zhang, R. Si, Y. Zou, Y. Y. Ma, J. C. Ho, Y. Q. Qu, *Nano Energy* **2022**, *104*, 107960.

[42] G. Henkelman, A. Arnaldsson, H. Jónsson, *Comput. Mater. Sci.* **2006**, *36*, 354.

[43] J. S. Lee, G. Nam, J. Sun, S. Higashi, H. W. Lee, S. Lee, W. Chen, Y. Cui, J. Cho, *Adv. Energy Mater.* **2016**, *6*, 1601052.

[44] S. C. Ren, L. Liu, F. D. Meng, Y. L. Liu, Y. S. Xie, H. B. Sun, Y. Yang, H. L. Yan, F. H. Wang, *Energy Storage Mater.* **2024**, *65*, 103086.

[45] a) M. Q. Yu, E. Budiyanto, H. Tüysüz, *Angew. Chem.-Int. Edit.* **2022**, *61*, 202103824; b) W. T. Hong, M. Risch, K. A. Stoerzinger, A. Grimaud, J. Suntivich, Y. Shao-Horn, *Energy Environ. Sci.* **2015**, *8*, 1404.